

Polymorphism and optical, magnetic and thermal properties of the either phyllo- or inosilicate-analogous borosulfate $\text{Cu}[\text{B}_2(\text{SO}_4)_4]$

Matthias Hämmer, Florian Pielhofer, Oliver Janka, Hirotaka Takahashi, Peter Gross, Rainer Pöttgen, Henning A. Höpfe

Angaben zur Veröffentlichung / Publication details:

Hämmer, Matthias, Florian Pielhofer, Oliver Janka, Hirotaka Takahashi, Peter Gross, Rainer Pöttgen, and Henning A. Höpfe. 2022. "Polymorphism and optical, magnetic and thermal properties of the either phyllo- or inosilicate-analogous borosulfate $\text{Cu}[\text{B}_2(\text{SO}_4)_4]$." *Dalton Transactions* 51 (8): 3104–15. <https://doi.org/10.1039/d1dt04090a>.



Polymorphism and optical, magnetic and thermal properties of the either phyllo- or inosilicate-analogous borosulfate $\text{Cu}[\text{B}_2(\text{SO}_4)_4]^\dagger\ddagger$

Matthias Hämmer,^a Florian Pielnhofer,^b Oliver Janka,^{c,d} Hirotaka Takahashi,^a Peter Gross,^a Rainer Pöttgen^d and Henning A. Höppe^{*a}

Two polymorphs of the borosulfate $\text{Cu}[\text{B}_2(\text{SO}_4)_4]$ can be selectively prepared by solvothermal syntheses. The crystal structures of inosilicate-analogous $\alpha\text{-Cu}[\text{B}_2(\text{SO}_4)_4]$ ($P\bar{1}$, no. 2, $a = 5.2636(2)$, $b = 7.1449(2)$, $c = 7.9352(2)$ Å, $\alpha = 73.698(2)^\circ$, $\beta = 70.737(2)^\circ$, $\gamma = 86.677(2)^\circ$, 65 parameters, $R_{\text{Bragg}} = 0.0052$) and the new phyllosilicate-analogous polymorph $\beta\text{-Cu}[\text{B}_2(\text{SO}_4)_4]$ ($P2_1/n$, no. 14, $a = 7.712(3)$, $b = 8.149(3)$, $c = 9.092(3)$ Å, $\beta = 111.22(1)^\circ$, 3829 independent reflections, 106 parameters, $wR_2 = 0.054$) are discussed. Further, the optical, magnetic and thermal properties of both polymorphs are investigated with focus on the role of the Cu^{2+} cation and its Jahn–Teller effect. The findings are confirmed by DFT calculations yielding insights in the stability of the synthesised polymorphs as well as a predicted γ -modification. Additionally, the crystal structures of two polymorphs of copper hydrogensulfate $\text{Cu}(\text{HSO}_4)_2\text{-I}$ ($P2_1/n$, no. 14, $a = 4.7530(2)$, $b = 8.5325(4)$, $c = 7.3719(3)$ Å, $\beta = 100.063(1)^\circ$, 1063 independent reflections, 55 parameters, $wR_2 = 0.052$) and $\text{Cu}(\text{HSO}_4)_2\text{-II}$ ($P\bar{1}$, no. 2, $a = 4.79.88(8)$, $b = 7.857(1)$, $c = 8.057(1)$ Å, $\alpha = 77.86(1)^\circ$, $\beta = 87.02(1)^\circ$, $\gamma = 89.82(1)^\circ$, 1044 independent reflections, 109 parameters, $wR_2 = 0.132$) as well as that of $\text{Cu}[\text{S}_2\text{O}_7]$ ($C2/c$, no. 15, $a = 6.6341(4)$, $b = 8.7302(5)$, $c = 9.0555(8)$ Å, $\beta = 104.763(3)^\circ$, 1117 independent reflections, 48 parameters, $wR_2 = 0.049$) are presented and the cyclosilicate-analogous borosulfate $\text{Cu}[\text{B}(\text{SO}_4)_2(\text{HSO}_4)]$ is fully characterised with respect to its optical and thermal properties.

Introduction

Borosulfates are an ever-expanding compound class and part of our systematic investigation of silicate-analogous materials including fluoroxyborates,¹ borates² and tungstates.³ Silicate-analogous materials comprise tetrahedral basic building units as the characteristic structural motif. The absence of an inversion centre within tetrahedra often leads to interesting optical properties as they foster non-centrosymmetric coordination environments around emitting cations and thus promote high

luminescence probabilities or even nonlinear optical properties if the whole structure lacks inversion symmetry.^{1,3–7} With the first crystalline borosulfate $\text{K}_5[\text{B}(\text{SO}_4)_4]$ discovered as recent as 2012,⁸ there are over seventy compounds characterised to date.^{7,9–15} Borosulfates may be classified as silicate-analogous¹⁶ in two ways: on the one hand, their anions consist most commonly¹⁵ of corner sharing borate and sulfate tetrahedra, solely. On the other hand, such structures can be understood by considering supertetrahedra TX_4 formed by a boron atom acting as centre T coordinated tetrahedrally by four SO_4 moieties X as frequently observed in the building unit $[\text{B}(\text{SO}_4)_4]^{5-}$. Consequently, the T:X ratio determines the anion's topology. Hence, the borosulfates can be classified by the dimensionality of the borosulfate anion, *i.e.* the connection of supertetrahedra. For that, Friedrich Liebau's classification of silicates is adapted.¹⁶ There are borosulfates with 0D anions like the cyclosilicate-analogous $\text{M}_2[\text{B}_2(\text{SO}_4)_6]$ ($\text{M} = \text{Y}, \text{La-Nd}, \text{Sm-Lu}, \text{Bi}$)^{5,6,17} or the nesosilicate-analogous $\text{K}_5[\text{B}(\text{SO}_4)_4]$,⁸ 1D anions like the inosilicate-analogous $(\text{NH}_4)_3[\text{B}(\text{SO}_4)_3]$,¹⁰ 2D anions like the phyllosilicate-analogous α - and $\beta\text{-M}[\text{B}_2(\text{SO}_4)_4]$ ($\text{M} = \text{Mg}, \text{Co}$)^{11,14,18} and 3D anions like the tectosilicate-analogous $\text{Bi}(\text{H}_3\text{O})[\text{B}(\text{SO}_4)_2]_4$.⁶ In contrast to these so-called conventional borosulfates, there are unconventional borosulfates comprising S–O–S or B–O–B bridges like $\text{Sr}[\text{B}_2(\text{SO}_4)_3(\text{S}_2\text{O}_7)]^9$

^aInstitut für Physik, Universität Augsburg, Universitätsstraße 1, 86159 Augsburg, Germany. E-mail: henning@ak-hoepp.de

^bInstitut für Anorganische Chemie, Universität Regensburg, Universitätsstraße 31, 93053 Regensburg, Germany

^cUniversität des Saarlandes, Anorganische Festkörperchemie, Campus C4 1, 66123 Saarbrücken, Germany

^dInstitut für Anorganische und Analytische Chemie, Westfälische Wilhelms-Universität Münster, Corrensstraße 30, 48149 Münster, Germany

† Electronic supplementary information (ESI) available: Microscope crystal pictures, crystallographic tables, details on Rietveld refinements, additional illustration of crystal structures, electrostatic calculations, geometric calculations, quantum chemical calculations, full IR spectra, fit and analyses of UV-Vis-NIR spectra, Tauc plots, thermal analyses. See DOI: 10.1039/d1dt04090a

‡ Dedicated to Prof. Wolfgang Beck on the occasion of his 90th birthday.

and $\text{Mg}_4[\text{B}_2\text{O}(\text{SO}_4)_6]^{18}$ violating Pauling's fourth¹⁹ and Loewenstein's rules,²⁰ respectively.

So far, only few borosulfates exhibit polymorphism: for $\text{Mg}[\text{B}_2(\text{SO}_4)_4]$ and $\text{Co}[\text{B}_2(\text{SO}_4)_4]$ two phyllosilicate-analogous polymorphs differing in the location of the metal cation within or in between the anionic layers are known,¹¹ $\text{Na}_5[\text{B}(\text{SO}_4)_4]$ shows two nesosilicate-analogous polymorphs²¹ and finally two polymorphs were described for the unconventional 0D borosulfates $\text{Mg}_4[\text{B}_2\text{O}(\text{SO}_4)_6]$ comprising B–O–B bonds¹⁸ and $\text{Mg}_3[\text{H}_2\text{O} \rightarrow \text{B}(\text{SO}_4)_3]_2$ forming a Lewis acid base adduct with water.¹⁵ However, in all cases the polymorphs feature the same dimensionality of the anionic substructure. For $\text{Mg}[\text{B}_2(\text{SO}_4)_4]$ and $\text{Co}[\text{B}_2(\text{SO}_4)_4]$, the polymorphism can be controlled by synthesis using the choice of reactant and solvent and the aging interval.¹¹ Moreover, it was shown that the respective reactant governs the bond formation in borosulfates for the cations of barium and strontium.^{9,12} Pure oleum promotes the formation of disulfate units, *i.e.* S–O–S bonds, a mixture of oleum and H_2SO_4 exclusively B–O–S bonds and pure H_2SO_4 B–O–B bonds within the respective borosulfates.

In 2018, the first two copper borosulfates $\text{Cu}[\text{B}_2(\text{SO}_4)_4]$ and $\text{Cu}[\text{B}(\text{SO}_4)_2(\text{HSO}_4)]$ were reported crystallising with inosilicate-analogous and cyclosilicate-analogous borosulfate anions, respectively. Besides the crystal structures, only the magnetic properties of both compounds had been investigated. Notably, phase pure samples could only be prepared of $\text{Cu}[\text{B}(\text{SO}_4)_2(\text{HSO}_4)]$ while $\text{Cu}[\text{B}_2(\text{SO}_4)_4]$ was obtained in mixtures with $\text{Cu}[\text{B}(\text{SO}_4)_2(\text{HSO}_4)]$ and a maximum content of 22% $\text{Cu}[\text{B}_2(\text{SO}_4)_4]$.²²

Most commonly, Cu^{2+} oxo salt compounds feature CuO_6 polyhedra.²³ Due to the $[\text{Ar}]3d^9$ electronic ground state of the Cu^{2+} cation the octahedral coordination environment is affected strongly by a Jahn–Teller distortion usually resulting in a (4 + 2) coordination with four – equatorial – Cu–O distances being shorter and two – apical – ones being longer. Nevertheless, the formation of a compressed octahedron with (2 + 4) coordination is equally likely according to the first order Jahn–Teller distortion – however, this is rarely found.^{23–27}

In our contribution, we address the phase pure synthesis of both, $\text{Cu}[\text{B}_2(\text{SO}_4)_4]$ – more precisely $\alpha\text{-Cu}[\text{B}_2(\text{SO}_4)_4]$ – and the new polymorph $\beta\text{-Cu}[\text{B}_2(\text{SO}_4)_4]$, crystallising in the monoclinic

space group $P2_1/n$, the elucidation of their crystal structures and the nature of the polymorphism as well as the investigation of their optical, thermal and magnetic properties. The findings are supported by the results of DFT calculations. For the sake of completeness and comparison, $\text{Cu}[\text{B}(\text{SO}_4)_2(\text{HSO}_4)]$ was also characterised with respect to its optical and thermal properties. As sort of by-catch, we also report on the first characterisation of two polymorphs $\text{Cu}(\text{HSO}_4)_2\text{-I}$ and $\text{Cu}(\text{HSO}_4)_2\text{-II}$ of copper hydrogen sulfate and of $\text{Cu}[\text{S}_2\text{O}_7]$.

Results and discussion

Syntheses

Both $\alpha\text{-Cu}[\text{B}_2(\text{SO}_4)_4]$ and $\beta\text{-Cu}[\text{B}_2(\text{SO}_4)_4]$ were synthesised solvothermally at 450 K from $\text{Cu}_2[(\text{OH})_2\text{CO}_3]$ and $\text{B}(\text{OH})_3$ in pure oleum (65% SO_3) or in a mixture of H_2SO_4 and oleum, respectively. The syntheses yielded colourless powders containing large single-crystals shown in Fig. S1.† Judging by the morphology of the crystals we observed two different kinds in the $\beta\text{-Cu}[\text{B}_2(\text{SO}_4)_4]$ sample and only one in $\alpha\text{-Cu}[\text{B}_2(\text{SO}_4)_4]$. The phase composition was checked by powder XRD after washing the products with anhydrous acetonitrile (Fig. 1). $\beta\text{-Cu}[\text{B}_2(\text{SO}_4)_4]$ was obtained with a side phase of $\alpha\text{-Cu}[\text{B}_2(\text{SO}_4)_4]$ while $\alpha\text{-Cu}[\text{B}_2(\text{SO}_4)_4]$ could be prepared as phase pure powder. The side phase was quantified by Rietveld analysis to 7 wt.-% (details in Table S1†). This agrees with the morphology differences observed by light microscopy showing two different single-crystal species. In contrast to earlier reports by Bruns *et al.*,²² the formation of $\text{Cu}[\text{B}(\text{SO}_4)_2(\text{HSO}_4)]$ was not observed for both syntheses. Consequently, the selective synthesis of a polymorph is governed by the SO_3 content of the solvent and the choice of the reactants. However, the SO_3 content and the synthesis temperature appear to be complementary parameters. Bruns *et al.*²² prepared $\text{Cu}[\text{B}(\text{SO}_4)_2(\text{HSO}_4)]$ containing an unidentified side phase from Cu_2O with 20% SO_3 at 450 K while we could synthesise $\text{Cu}[\text{B}(\text{SO}_4)_2(\text{HSO}_4)]$ from $\text{Cu}_2[(\text{OH})_2\text{CO}_3]$ with 65% SO_3 at 400 K as an almost colourless very pale blueish powder. Rietveld refinement revealed the presence of a 2 wt.-% side phase of CuSO_4 (Fig. S2 and Table S2†).

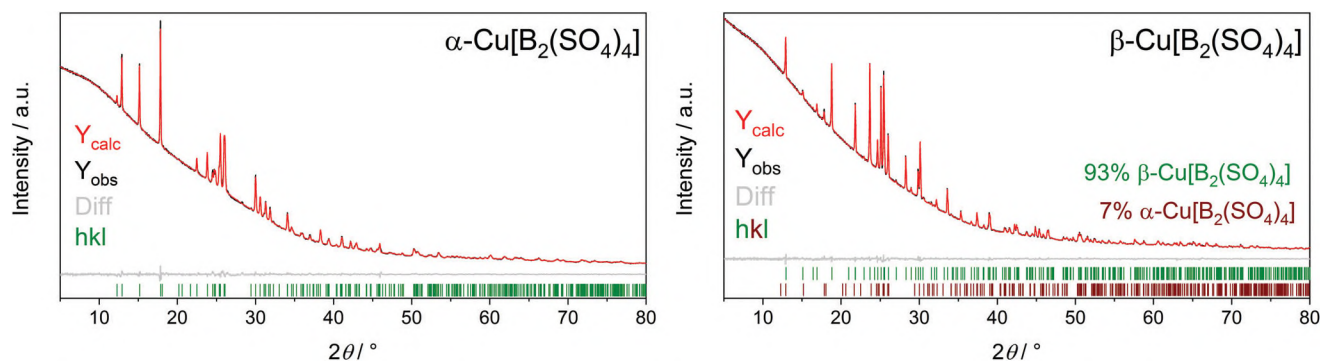


Fig. 1 Rietveld-Refinement of $\alpha\text{-Cu}[\text{B}_2(\text{SO}_4)_4]$ confirming the phase purity (left) and $\beta\text{-Cu}[\text{B}_2(\text{SO}_4)_4]$ showing contents of 93% for the main phase $\beta\text{-Cu}[\text{B}_2(\text{SO}_4)_4]$ and 7% for the side phase $\alpha\text{-Cu}[\text{B}_2(\text{SO}_4)_4]$ (right); further details can be found in Table S1.†

Crystal structures

Cu(HSO₄)₂. In preliminary experiments, we obtained single-crystals of two modifications of the as yet unreported compound Cu(HSO₄)₂ (Tables S3–S5†). The polymorph Cu(HSO₄)₂-I crystallises in the monoclinic space group *P*2₁/*n* (no. 14) and two formula units per unit cell depicted in Fig. S3.† Distorted CuO₆ octahedra are coordinated by six monodentate hydrogensulfate anions (Fig. S4†) held together by moderately strong hydrogen bonds with a donor acceptor distance of 262.3(2) pm (Fig. S5†). Cu(HSO₄)₂-II crystallises in the triclinic crystal system with space group *P*1̄ (no. 2) and two formula units per unit cell depicted in Fig. S6.† Two crystallographically distinct distorted CuO₆ octahedra are connected *via* common corners yielding chains along *b*. Each copper atom is coordinated by six monodentate hydrogensulfate anions with two anions shared between Cu(1) and Cu(2) (Fig. S7†). All three unprotonated oxygen atoms within the hydrogensulfate anions are coordinating copper atoms. Consequently, the hydrogensulfate anions connect the Cu–O chains forming layers in the *ab* plane. These planes are linked *via* moderately strong hydrogen bonds with a donor acceptor distance of 265.4(7) pm (Fig. S8†) to a network. Further, weak hydrogen bonds occur alongside the Cu–O chains with donor acceptor distances of 330.5(6) pm (Fig. S9†). These values for the hydrogen bonds should be treated with caution due to the limited data quality. The deviations from the octahedral or tetrahedral symmetry Δ_{oct} or Δ_{tet} were calculated by the method of Balić-Žunić and Makovicky based on all ligands enclosing spheres on experimental data.^{28,29} All hydrogensulfate tetrahedra can be considered regular³⁰ with deviations of 0.15% for Cu(HSO₄)₂-I and 0.08% and 0.09% for Cu(HSO₄)₂-II. The CuO₆ polyhedra deviate significantly from the octahedral symmetry with deviations of 29.1% in Cu(HSO₄)₂-I and 31.9% and 34.4% in Cu(HSO₄)₂-II. This is due to the Jahn–Teller distortion which is discussed in detail in the following in comparison to Cu[B₂(SO₄)₄]. The electrostatic reasonability of the crystal structures of both Cu(HSO₄)₂ modifications and all coordination numbers were confirmed by calculations based on the MAPLE concept (Madelung Part of Lattice Energy) presented in Tables S6–S9.†^{31–34}

Cu[S₂O₇]. During further preliminary experiments, single-crystals of Cu[S₂O₇] were obtained and used for single-crystal XRD (Tables S10–S12†) in agreement with an earlier report.³⁵ It crystallises in the monoclinic space group *C*2/*c* (no. 15) and four formula units per unit cell as depicted in Fig. S10.† Jahn–Teller distorted elongated CuO₆ octahedra are coordinated by two monodentate and two bidentate [S₂O₇]²⁻ anions (Fig. S11†) with the bridging oxygen atom being the only one not coordinating any copper atom. Along [010] alternating anion and cation layers are formed (Fig. S12†). The sulfate tetrahedron can be considered regular³⁰ with $\Delta_{\text{tet}} = 0.10\%$ while the CuO₆ polyhedron deviates from the octahedral symmetry with $\Delta_{\text{oct}} = 26.8\%$. Again, this deviation is discussed in detail in the following in comparison to Cu[B₂(SO₄)₄]. Finally, the electrostatic reasonability of the

crystal structure and all coordination numbers were confirmed by calculations based on the MAPLE concept (Tables S13 and S14†).^{31–34}

α-Cu[B₂(SO₄)₄]. α-Cu[B₂(SO₄)₄] crystallises in the triclinic space group *P*1̄ (no. 2) and one formula unit per unit cell (Fig. 2a). The borosulfate anion forms exclusively B(SO₄)₄ supertetrahedra consisting of tetrahedrally coordinated sulfate and borate anions. The borate and sulfate tetrahedra can all be classified regular³⁰ with deviations of 0.7%, 1.2% and 1.8% for B1O₄, S1O₄ and S2O₄, respectively. The anion forms loop branched *vierer* single chains with the Niggli formula $\frac{1}{\infty}[\text{B}(\text{SO}_4)_{4/2}]^-$ and can therefore be described as a chain of edge sharing supertetrahedra (Fig. 2b). The Cu²⁺ cation is octahedrally coordinated by six oxygen atoms. Six sulfate units coordinate in a monodentate fashion stemming from four different anion chains, *i.e.* two chains provide two oxygen atoms and two provide one (Fig. 2c). Jahn–Teller distortion leads to enlarged apical Cu–O distances. This is towards the anion chains coordinating by one sulfate anion, only. The Cu–O distances are reasonably close to the sum of ionic radii (Table S15†) with a (2 + 2 + 2) coordination, a subclass of the (4 + 2) coordination introduced earlier.²³ As expected, the CuO₆ octahedra deviate significantly from the ideal symmetry with $\Delta_{\text{oct}} = 22\%$. Additionally, the distance of the copper atom from the centroid of the CuO₆ octahedron was calculated by the method of Balić-Žunić and Makovicky, too.^{28,29} The Cu²⁺ cation actually centres the centroid of the octahedron (calculated deviation: 0.0(1) pm). Consequently, the Jahn–Teller distortion being a ligand field effect influences the shape of the octahedron and not the location of the Cu²⁺ cation. The latter was recently reported for the lone pair effect of Bi³⁺ cations in Bi₂[B₂(SO₄)₆].⁶ The electrostatic reasonability of the crystal structure of α-Cu[B₂(SO₄)₄] was confirmed by calculations based on the MAPLE concept.^{31–34} The MAPLE values of α-Cu[B₂(SO₄)₄] were calculated and compared to the sum of the MAPLE values of CuSO₄, B₂S₂O₉ and SO₃, respectively (Table S16†). The deviation is well below 1%, which is our empirical benchmark for electrostatic consistency. Furthermore, the calculations confirm all coordination numbers discussed earlier (Table S17†).

According to the TX formalism introduced earlier, the B : S ratio of 1 : 2 in α-Cu[B₂(SO₄)₄] indicates a three-dimensional anion. However, α-Cu[B₂(SO₄)₄] shows exclusively the connection pattern of SiS₂³⁶ resulting in the one dimensional anion.

β-Cu[B₂(SO₄)₄]. β-Cu[B₂(SO₄)₄] crystallises in the monoclinic crystal system with space group *P*2₁/*n* (no. 14) and two formula units per unit cell (Tables S18–S20†). The unit cell is depicted in Fig. 2d. The borosulfate anion forms exclusively B(SO₄)₄ supertetrahedra. The supertetrahedra alternately share edges and corners. Consequently, they form $\frac{2}{\infty}[\text{B}(\text{SO}_4)_{4/2}]^-$ layers comprising of *zwölfer* and *vierer* rings. Each *zwölfer* ring is connected to four other *zwölfer* rings directly and to another two *via vierer* rings. Consequently, the anion has phyllosilicate topology according to Liebau's nomenclature of silicates.¹⁶ More precisely, the anion is described by the Niggli formula

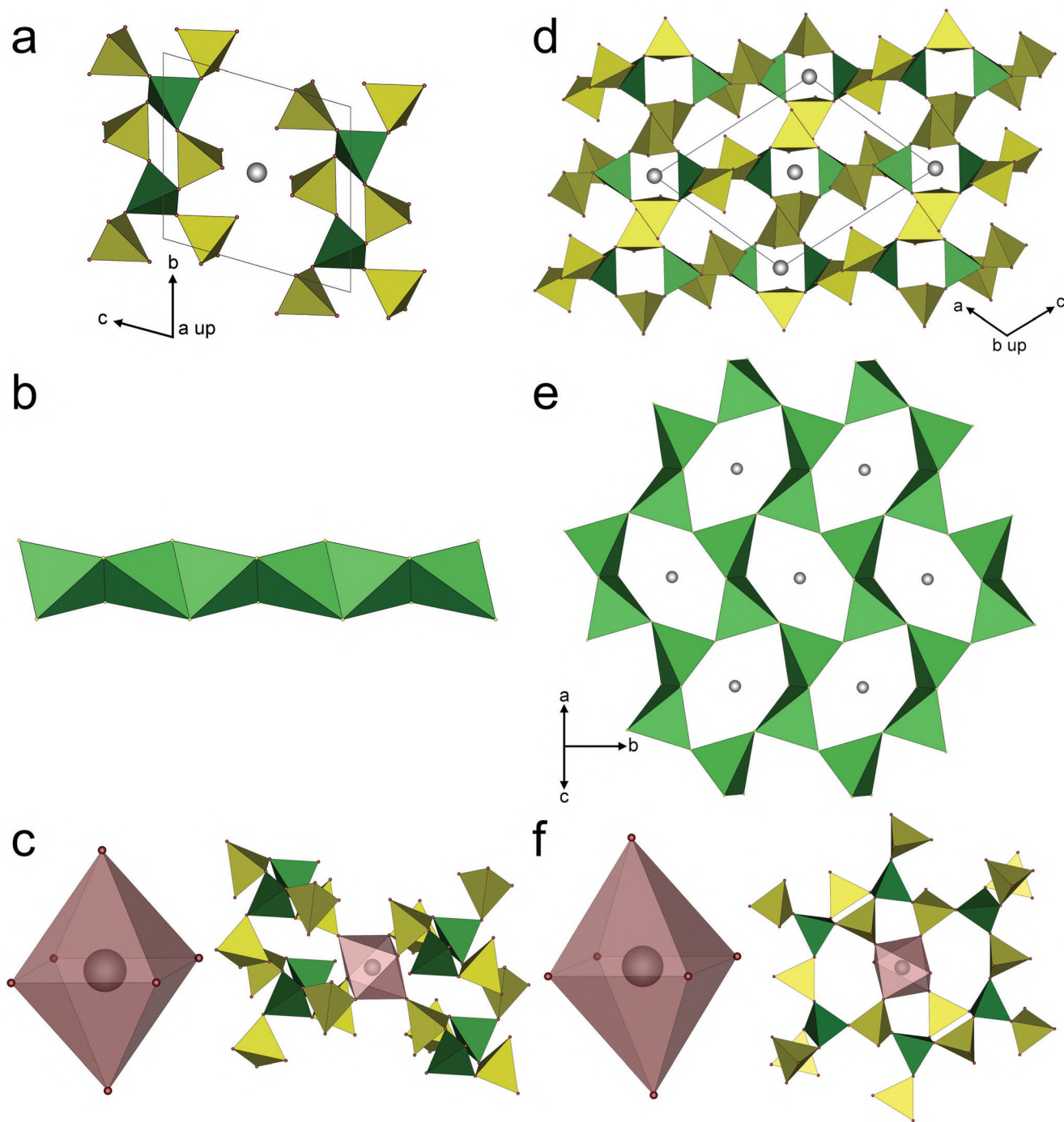


Fig. 2 The following colour code has been used for all pictures: copper atoms are grey, borate tetrahedra green, sulfate tetrahedra yellow, oxygen atoms red and $B(SO_4)_4$ supertetrahedra light green; (a) unit cell of $\alpha\text{-Cu}[B_2(SO_4)_4]$ viewed along (100); (b) the ${}^2_{\infty}[B(SO_4)_{4/2}]^-$ anion chain in $\alpha\text{-Cu}[B_2(SO_4)_4]$ depicted as edge sharing $B(SO_4)_4$ (c) octahedral coordination environment of the Cu^{2+} cations in $\alpha\text{-Cu}[B_2(SO_4)_4]$ (left) and the location of those octahedra between four anionic chains (right); (d) unit cell $\beta\text{-Cu}[B_2(SO_4)_4]$ viewed along (010); the ${}^2_{\infty}[B(SO_4)_{4/2}]^-$ anionic layers are shown in side view; (e) the layers in $\beta\text{-Cu}[B_2(SO_4)_4]$ formed by corner and edge sharing supertetrahedra $B(SO_4)_4$ resulting in *sechser* rings with the Cu^{2+} cations located inside and corner sharing dimers of supertetrahedra; (f) octahedral coordination environment of the Cu^{2+} cations in $\beta\text{-Cu}[B_2(SO_4)_4]$ (left) and the location of those octahedra in the *zwölfer* ring (right); the two additional oxygen atoms belong to the anion layers above and below, respectively.

${}^2_{\infty}\{[B(SO_4)_4^e(SO_4)_4^c]_{2/2}^-\}$ (e = edge sharing, c = corner sharing) by considering the supertetrahedron $B(SO_4)_4$ as building unit.¹¹ The supertetrahedra form *sechser* rings *via* the shared

corners and dimers *via* shared edges (Fig. 2e). The Cu^{2+} cation is octahedrally coordinated by six oxygen atoms, *i.e.* monodentately by six sulfate tetrahedra. Four sulfate moieties

belong to one anion layer with the Cu^{2+} cation inside the *zwölfer* ring and the residual two belong to the layers above and below, respectively (Fig. 2f). Consequently, a network is formed. The Cu–O distances are reasonably close to the sum of ionic radii (Table S21†). Further, Jahn–Teller distortion leads to elongation of the apical Cu–O distances. Again, the coordination of the Cu^{2+} cation can be described as (2 + 2 + 2). However, the difference between the two sets of equatorial distances is much smaller than they differ from the apical ones.

As expected, the CuO_6 octahedra not connected to further CuO_6 octahedra deviate significantly from the ideal symmetry with $\Delta_{\text{oct}} = 35\%$ with the Cu^{2+} cation 0.0(1) pm away from the centroid. This is larger than the insignificant deviation for $\alpha\text{-Cu}[\text{B}_2(\text{SO}_4)_4]$ ($\Delta_{\text{oct}} = 22\%$, deviation from centroid: 0.0(1) pm). Further, the elongation of the apical Cu–O distances is smaller in $\alpha\text{-Cu}[\text{B}_2(\text{SO}_4)_4]$, too. The Jahn–Teller distortion in $\beta\text{-Cu}[\text{B}_2(\text{SO}_4)_4]$ is more pronounced compared to $\alpha\text{-Cu}[\text{B}_2(\text{SO}_4)_4]$. In comparison to $\text{Cu}(\text{HSO}_4)_2$ and $\text{Cu}[\text{S}_2\text{O}_7]$, the magnitude of the Jahn–Teller distortion can be ranked in increasing order as follows by either Δ_{oct} or the tetragonality³⁷ T given in parentheses and discussed in detail with the optical properties in the following: $\alpha\text{-Cu}[\text{B}_2(\text{SO}_4)_4]$ (0.89), $\text{Cu}[\text{S}_2\text{O}_7]$ (0.86), $\text{Cu}(\text{HSO}_4)_2\text{-I}$ (0.84), $\text{Cu}(\text{HSO}_4)_2\text{-II}$ (0.83), $\beta\text{-Cu}[\text{B}_2(\text{SO}_4)_4]$ (0.82). This can be explained by the coordination environments and the different cooperative effects²⁴ between the anionic substructure and the copper(II) cation. This effect appears to be the strongest in $\beta\text{-Cu}[\text{B}_2(\text{SO}_4)_4]$ and can be explained by the rigidity of the phyllosilicate-analogous anion. In contrast to the other structures, the anionic substructure of $\beta\text{-Cu}[\text{B}_2(\text{SO}_4)_4]$ is strongly affected by the Jahn–Teller distortion. Apparently, the distortion of the anionic substructure enhances a larger Jahn–Teller distortion due to cooperative effects. On the other hand, such cooperative effects are apparently much weaker for $\alpha\text{-Cu}[\text{B}_2(\text{SO}_4)_4]$ and its anionic chains. In comparison, they are larger in $\text{Cu}(\text{HSO}_4)_2\text{-II}$ with hydrogensulfate anions exclusively around the Cu–O chains than in $\text{Cu}(\text{HSO}_4)_2\text{-I}$ with an almost spherical coordination of copper atoms by hydrogensulfate anions. Similarly, the cooperative effects of the disulfate anions appear to be even smaller than for hydrogensulfate anions.

The borate and sulfate tetrahedra in $\beta\text{-Cu}[\text{B}_2(\text{SO}_4)_4]$ can all be classified regular³⁰ with deviations of 0.4%, 0.2% and 0.7% for B_1O_4 , S_1O_4 and S_2O_4 , respectively. The deviations calculated from the data determined by Rietveld refinement can be found in Table S22.† Further, the electrostatic reasonability of the crystal structure of $\beta\text{-Cu}[\text{B}_2(\text{SO}_4)_4]$ was confirmed by calculations based on the MAPLE concept.^{31–34} The MAPLE values of $\beta\text{-Cu}[\text{B}_2(\text{SO}_4)_4]$ were calculated and compared to the sum of the MAPLE values of CuSO_4 , B_2O_3 and SO_3 (Table S16†). The deviation is well below 1%. Furthermore, the calculations confirm all coordination numbers discussed earlier (Tables S23 and S24†). The effective coordination numbers calculated by the MAPLE calculations also show the influence of the Jahn–Teller distortion – especially in comparison to the homeotypic $\beta\text{-M}[\text{B}_2(\text{SO}_4)_4]$ ($\text{M} = \text{Mg}, \text{Co}$).¹¹ Additionally, these calculations confirm the stronger effect of the Jahn–Teller distortion

in $\beta\text{-Cu}[\text{B}_2(\text{SO}_4)_4]$ compared to $\alpha\text{-Cu}[\text{B}_2(\text{SO}_4)_4]$ and the ranking of the Jahn–Teller distortion including both modifications of $\text{Cu}(\text{HSO}_4)_2$ and $\text{Cu}[\text{S}_2\text{O}_7]$ as discussed above (Tables S7–S9, S14, S17, S23 and S24†).

According to the sum formula and the TX formalism introduced in the introduction, the B:S ratio of 1:2 indicates a three-dimensional anionic network. However, the alternation of edge and corner sharing supertetrahedra combines both connecting patterns of three-dimensional networks like in SiO_2 ³⁸ and the chain like in SiS_2 ³⁶ resulting in the layered two-dimensional anion.

According to our results, $\beta\text{-Cu}[\text{B}_2(\text{SO}_4)_4]$ crystallises isotypically to $\text{Mn}[\text{B}_2(\text{SO}_4)_4]$ and homeotypic – differing in the orientation of one sulfate tetrahedron, only – to $\text{Zn}[\text{B}_2(\text{SO}_4)_4]$,³⁹ $\beta\text{-Mg}[\text{B}_2(\text{SO}_4)_4]$ and $\beta\text{-Co}[\text{B}_2(\text{SO}_4)_4]$.^{11,14} Further, the borosulfates $\alpha\text{-Mg}[\text{B}_2(\text{SO}_4)_4]$ ¹⁸ and $\alpha\text{-Co}[\text{B}_2(\text{SO}_4)_4]$ ^{11,14} have an analogous sum formula and similar structures. They contain also phyllosilicate-analogous anions formed by *zwölfer* and *vierer* rings. The structures deviate in the position of the respective cation being located above and underneath the *zwölfer* rings between two layers instead inside the rings in $\beta\text{-Cu}[\text{B}_2(\text{SO}_4)_4]$. This configuration – “cation between layers” in contrast to “cation within layers” – appears to be less stable for $\text{Cu}[\text{B}_2(\text{SO}_4)_4]$, maybe due to the Jahn–Teller distortion requiring two different sets of four short equatorial and two long apical Cu–O distances. The equatorial and apical cation oxygen distances deviate only slightly from each other in $\alpha\text{-Mg}[\text{B}_2(\text{SO}_4)_4]$ ¹⁸ (205–206 pm, 203 pm, $\sum\text{IR} = 207$ pm)⁴⁰ and $\alpha\text{-Co}[\text{B}_2(\text{SO}_4)_4]$ ¹¹ (209 pm, 204 pm, $\sum\text{IR} = 210$ pm).⁴⁰ If the cations are hosted between two layers, their coordination is influenced by these two while in $\beta\text{-Cu}[\text{B}_2(\text{SO}_4)_4]$ in total three layers contribute to the coordination sphere of the cations. Consequently, there is little freedom for the Jahn–Teller distortion to take shape in the former whereas the higher number of anion layers involved in the Cu^{2+} coordination in $\beta\text{-Cu}[\text{B}_2(\text{SO}_4)_4]$ provides more flexibility for the distortion. This is confirmed by our DFT calculations including a hypothetical structure denoted as “ $\gamma\text{-Cu}[\text{B}_2(\text{SO}_4)_4]$ ” where the cations are localised between the anionic layers isotypic to $\alpha\text{-Co}[\text{B}_2(\text{SO}_4)_4]$ in the monoclinic space group $C2/c$ (no. 15). According to the optimised structures from DFT (lattice parameters and cell volumes in Table S25†), the α -modification is the most stable of the three investigated models. It is favoured over $\beta\text{-Cu}[\text{B}_2(\text{SO}_4)_4]$ by 6.3 kJ mol^{−1}. The hypothetical $\gamma\text{-Cu}[\text{B}_2(\text{SO}_4)_4]$ exhibits a similar density compared to $\alpha\text{-Cu}[\text{B}_2(\text{SO}_4)_4]$ and is further 6.6 kJ mol^{−1} above the β -polymorph (Fig. 3a). In $\gamma\text{-Cu}[\text{B}_2(\text{SO}_4)_4]$, the CuO_6 octahedra in a fully relaxed structural model exhibit shorter apical than equatorial Cu–O distances, therefore being compressed instead of elongated as found for the α - and β -polymorphs (Fig. 3b). This rather unusual (2 + 4) coordination environment for Cu(II), which is found e.g. in $\text{Cu}_3\text{Mo}_2\text{O}_9$ ²⁷ or $\text{Cu}_3\text{Cr}_4(\text{PO}_4)_6$ ²⁶ can be understood as the consequence of the dilemma described above with the rigid borosulfate anion preventing a significant elongation of the CuO_6 octahedra. A tendency towards compressed octahedra is also present in $\alpha\text{-Mg}[\text{B}_2(\text{SO}_4)_4]$ ($T = 1.01$) and $\alpha\text{-Co}[\text{B}_2(\text{SO}_4)_4]$ ($T =$

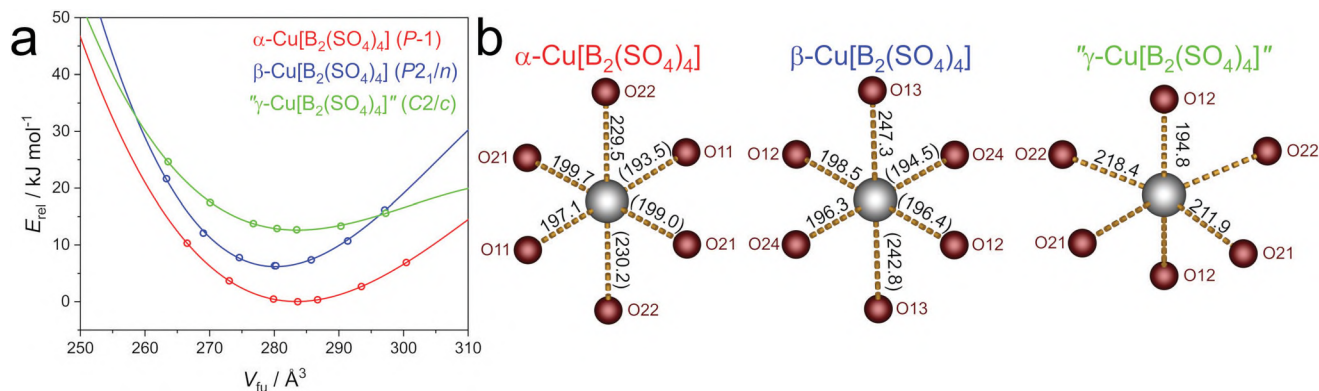


Fig. 3 (a) Energy versus volume plots for α -Cu[B₂(SO₄)₄] (*P* $\bar{1}$), β -Cu[B₂(SO₄)₄] (*P*2₁/*n*, “cation within layer”) and a hypothetical γ -Cu[B₂(SO₄)₄] (*C*2/*c*, “cation between layer”); (b) CuO₆ octahedra in the DFT optimised structures of α -Cu[B₂(SO₄)₄], β -Cu[B₂(SO₄)₄] and γ -Cu[B₂(SO₄)₄]; the Cu–O distances are given in pm from the DFT calculations and from the SC-XRD data (in parentheses, α -Cu[B₂(SO₄)₄],²² β -Cu[B₂(SO₄)₄]: this work); the tetragonality *T* (discussed in detail with the optical properties) amounts to 0.86, 0.80 and 1.04 for α -Cu[B₂(SO₄)₄], β -Cu[B₂(SO₄)₄] and γ -Cu[B₂(SO₄)₄], respectively.

1.02) discussed above. However, due to the rather small energetic difference of the hypothetical “cation between layer”-model γ -Cu[B₂(SO₄)₄] to the β -modification, we predict the existence of this third polymorph of Cu[B₂(SO₄)₄] with a peculiar Cu(II) coordination. The DFT-optimised crystal structures are available in the ESI† as cif-files.

Cu[B(SO₄)₂(HSO₄)]. The crystal structure of Cu[B(SO₄)₂(HSO₄)] was reported by Bruns *et al.* from single-crystal data at 173 K.²² Once again, the Cu²⁺ cation is coordinated by six oxygen atoms forming a Jahn–Teller distorted elongated octahedron. The octahedra deviate significantly from the ideal symmetry with deviations of 37.3% and 38.9% for Cu(1) and Cu(2), respectively. The cyclosilicate-analogous borosulfate anion comprises non-condensed dimers of edge sharing supertetrahedra – similar to the ones found in M₂[B₂(SO₄)₆]

(M = Y, La–Nd, Sm–Lu, Bi)^{5,6,17} – with additional hydrogen atoms at opposing terminal corners.

Optical properties

Infrared spectroscopy. The infrared spectra of α -Cu[B₂(SO₄)₄] and β -Cu[B₂(SO₄)₄] are shown in Fig. 4a in the region of 1600–400 cm⁻¹ (full spectra in Fig. S13†). The spectrum of β -Cu[B₂(SO₄)₄] agrees well with those of the homeotypic β -Co[B₂(SO₄)₄] and β -Mg[B₂(SO₄)₄]¹¹ and the calculations for β -Co[B₂(SO₄)₄]¹⁴ and Ca[B₂(SO₄)₄].⁴¹ The asymmetric stretching modes $\nu_{\text{asym.}}$ (S–O) appear at 1371, 1339, 1193 and 1183 cm⁻¹. The subsequent bands between 1160 and 970 cm⁻¹ can be assigned to $\nu_{\text{asym./sym.}}$ (B–O) and are followed by $\nu_{\text{sym.}}$ (S–O) at 870 cm⁻¹. Below the spectrum is governed by bending vibrations, namely the asymmetric bending vibrations

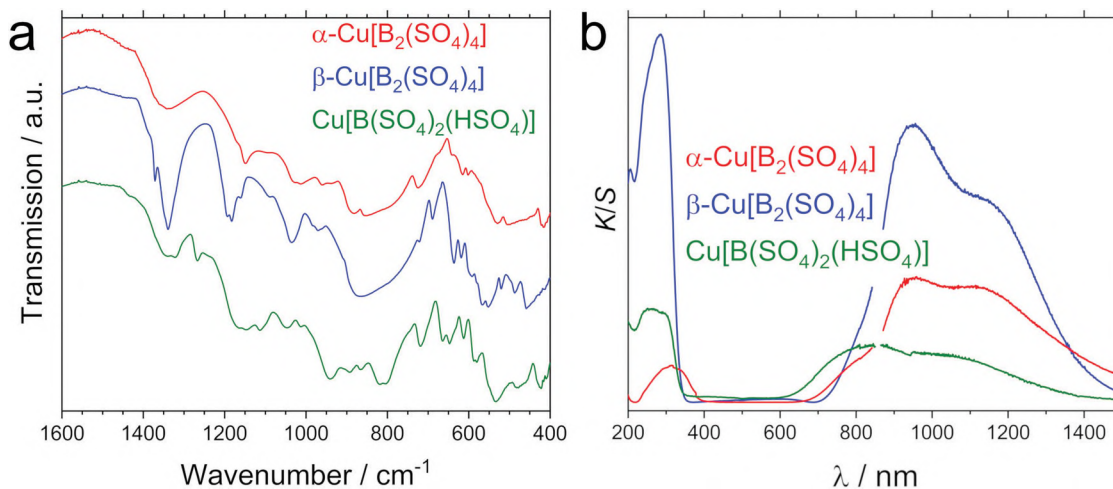


Fig. 4 (a) Infrared spectra of α -Cu[B₂(SO₄)₄], β -Cu[B₂(SO₄)₄] and Cu[B(SO₄)₂(HSO₄)]: the full spectra can be found in Fig. S13;† (b) UV-Vis-NIR spectra of α -Cu[B₂(SO₄)₄], β -Cu[B₂(SO₄)₄] and Cu[B(SO₄)₂(HSO₄)]: the spectra are broken around 850 nm due to the change of detector within the measuring device.

$\delta_{\text{asym.}}(\text{O-S-O, O-B-O, S-O-B})$ between 720 and 550 cm^{-1} and $\delta_{\text{asym.}}(\text{O-S-O, S-O-Cu})$ below. For $\alpha\text{-Cu[B}_2(\text{SO}_4)_4]$, calculated IR modes were reported by Bruns *et al.*²² They agree roughly with our experimental ones. The asymmetric stretching modes $\nu_{\text{asym.}}(\text{S-O})$ at 1338 and 1147 cm^{-1} are followed by $\nu_{\text{asym./sym.}}(\text{B-O})$ between 1030 and 937 cm^{-1} and the symmetric stretching vibrations S-O at 884 and 855 cm^{-1} . Then, $\delta(\text{O-S-O, O-B-O, S-O-B})$ appear between 724 and 602 cm^{-1} . The deformation modes of the CuO_6 octahedra are overlapped by further $\delta(\text{O-S-O})$ vibrations at 529, 503 and 417 cm^{-1} .

Further, the IR spectrum of $\text{Cu[B}(\text{SO}_4)_2(\text{HSO}_4)]$ depicted in Fig. 4a is in good agreement with the calculated one reported by Bruns *et al.*²² In contrast to $\text{Cu[B}_2(\text{SO}_4)_4]$, the asymmetric O-H stretching and the asymmetric and symmetric S-O-H bending modes are present at 2435, 1340 and 1230 cm^{-1} , respectively. They are followed by the asymmetric S-O stretching modes at 1265 and 1146 cm^{-1} as well as the symmetric one at 1164 cm^{-1} . The three bands at 1045, 1014 and 940 cm^{-1} can be assigned to the asymmetric B-O stretching vibrations. Below, the spectrum is again governed by bending vibrations like the S-O-H bending at 891 cm^{-1} , the O-B-O bending at 820 cm^{-1} , $\delta(\text{O-S-O, S-O-B})$ between 660 and 550 cm^{-1} and $\delta(\text{O-S-O, S-O-Cu})$ below.

UV-Vis-NIR spectroscopy. The powder reflectance spectra of $\alpha\text{-Cu[B}_2(\text{SO}_4)_4]$ and $\beta\text{-Cu[B}_2(\text{SO}_4)_4]$ are shown in Fig. 4b in the range from 200 nm to 1500 nm. Besides the fundamental absorption due to the bandgap of the samples in the UV regime a broad absorption band between 700 nm and 1300 nm can be found. The latter can be attributed to the d-d transitions of the Cu^{2+} cation. The spectra are in line with colourless powders. According to ligand field theory and the Jahn-Teller effect three possible d-d transitions may be recorded in $\text{Cu[B}_2(\text{SO}_4)_4]$: $a_{1g} \rightarrow b_{1g}$, $b_{2g} \rightarrow b_{1g}$ and $e_g \rightarrow b_{1g}$.⁴² The respective energy scheme is sketched in Fig. S14.† The simplification of assuming D_{4h} symmetry, *i.e.* a (4 + 2) coordination of Cu^{2+} is legitimate since the further splitting of states due to the actual (2 + 2 + 2) coordination can be expected to be too small to influence the resulting reflectance spectra significantly. Consequently, the ligand field splitting energy Δ and the Jahn-Teller energy E_{JT} can be derived directly from the spectra (Fig. S14.†). The transitions could be located at 1.07 eV (1163 nm), 1.38 eV (900 nm) and 1.65 eV

(752 nm) for $\alpha\text{-Cu[B}_2(\text{SO}_4)_4]$ and 1.08 eV (1147 nm), 1.39 eV (895 nm) and 1.61 eV (769 nm) for $\beta\text{-Cu[B}_2(\text{SO}_4)_4]$ using three Gaussian fits of the measured spectra, respectively (Fig. S15 and S16.†). Hence, there are ligand field splitting energies Δ of 11 116 cm^{-1} and 11 171 cm^{-1} and Jahn-Teller energies E_{JT} of 2149 cm^{-1} and 2179 cm^{-1} for $\alpha\text{-Cu[B}_2(\text{SO}_4)_4]$ and $\beta\text{-Cu[B}_2(\text{SO}_4)_4]$, respectively. These values are compared to other Cu^{2+} compounds from literature in Table S26.† Borosulfates are known to show weak ligand field splitting.^{11,18} Consequently, the ligand field splitting energies are smaller than for the hexaqua complex $[\text{Cu}^{\text{II}}(\text{OH}_2)_6]^{2+}$ (13 000 cm^{-1}).^{37,43} However, the ligand field splitting is larger than for respective fluorides or sulfates (9100 cm^{-1}).⁴⁴ E_{JT} is – in agreement with the discussion above – larger for $\beta\text{-Cu[B}_2(\text{SO}_4)_4]$ compared to $\alpha\text{-Cu[B}_2(\text{SO}_4)_4]$ confirming a stronger Jahn-Teller effect. The comparison with other Cu^{2+} compounds using Δ_{oct} appears to be not straightforward. The tetragonality T^{37} – roughly following E_{JT} – appears to be better suited to compare the ‘strength’ of the Jahn-Teller distortion (Table S26.†). The same holds for $\text{Cu[B}(\text{SO}_4)_2(\text{HSO}_4)]$ (Fig. 4b and Fig. S17.†) with its three transitions located at 1.21 eV (1022 nm), 1.53 eV (809 nm) and 1.74 eV (714 nm). The large energy of the last transition explains the pale blue appearance of the measured powder – especially in comparison to colourless $\text{Cu[B}_2(\text{SO}_4)_4]$. The large E_{JT} of 2447 cm^{-1} can be explained by the small tetragonality factor T both indicating a strong Jahn-Teller effect (Table S26.†). The ligand field splitting energy of 12 355 cm^{-1} is larger than the one for both polymorphs of $\text{Cu[B}_2(\text{SO}_4)_4]$ but still smaller than for $[\text{Cu}^{\text{II}}(\text{OH}_2)_6]^{2+}$ (13 000 cm^{-1}).^{37,43}

All three spectra show transitions from the valence to the conduction band in the UV regime. The band gaps were estimated using Tauc plots (Fig. S18–S20.†). The experimental values are 3.33(1), 3.82(1) and 3.76(1) eV for $\alpha\text{-Cu[B}_2(\text{SO}_4)_4]$, $\beta\text{-Cu[B}_2(\text{SO}_4)_4]$ and $\text{Cu[B}(\text{SO}_4)_2(\text{HSO}_4)]$, respectively.

Although near infrared luminescence is known for Cu^{2+} containing silicates⁴⁵ no emission could be observed for both $\alpha\text{-Cu[B}_2(\text{SO}_4)_4]$ and $\beta\text{-Cu[B}_2(\text{SO}_4)_4]$ up to 1500 nm.

Magnetic properties

The temperature dependent magnetic susceptibilities (χ) and the inverse (χ^{-1}) of both measured samples are shown in Fig. 5. The inverse susceptibilities were fitted in the tempera-

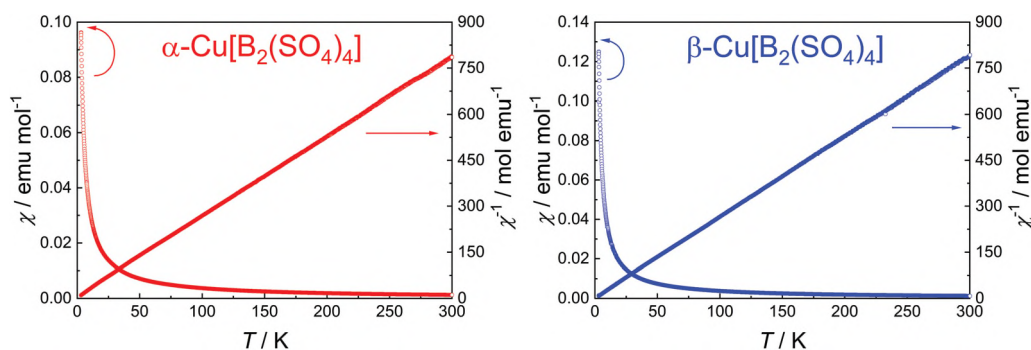
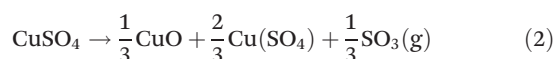
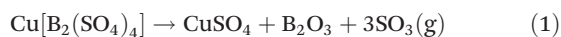


Fig. 5 Magnetic properties (χ and χ^{-1} data) of $\alpha\text{-Cu[B}_2(\text{SO}_4)_4]$ (1) (left) and a mixture of 93% $\beta\text{-Cu[B}_2(\text{SO}_4)_4]$ and 7% $\alpha\text{-Cu[B}_2(\text{SO}_4)_4]$ (2) (right).

ture range from 50–300 K *via* the Curie–Weiss law, using the corrected data. The effective magnetic moments were calculated to be $\mu_{\text{eff}} = 1.76(1)\mu_{\text{B}}$ for (1) and $\mu_{\text{eff}} = 1.74(1)\mu_{\text{B}}$ for the mixture (2). For Cu^{2+} (d^9), the calculated effective magnetic moment is $\mu_{\text{eff}} = 1.73\mu_{\text{B}}$, and therefore in excellent agreement with the two samples, thus confirming the oxidations state of the Cu^{2+} cations. The Weiss constants are $\theta_{\text{p}} = -3.5(1)$ K (1) and $\theta_{\text{p}} = -0.9(1)$ K (2) indicating only very weak (antiferro)magnetic interactions in the paramagnetic temperature regime, in line with the absence of magnetic ordering. Despite the crystallographic variations between both polymorphs, no significant differences in their magnetic properties were found.

Thermal analyses

The thermal decomposition of $\text{Cu}[\text{B}_2(\text{SO}_4)_4]$ was investigated by thermogravimetric analysis (TGA, Fig. 6), differential thermal analysis (DTA, Fig. S21†) under nitrogen atmosphere and temperature programmed X-ray powder diffraction (TPXRD, Fig. S22†) inside sealed argon filled glass capillaries. Due to a loss of crystallinity during the TPXRD measurements, samples of both $\alpha\text{-Cu}[\text{B}_2(\text{SO}_4)_4]$ and $\beta\text{-Cu}[\text{B}_2(\text{SO}_4)_4]$ were heated and the residual powder was investigated by powder XRD as well as the residue of the TGA measurement, additionally (Fig. S23–S26†). Both $\alpha\text{-Cu}[\text{B}_2(\text{SO}_4)_4]$ and $\beta\text{-Cu}[\text{B}_2(\text{SO}_4)_4]$ decompose at 460 K. A chemically plausible decomposition process follows the reaction eqn (1)–(3).



The expected mass losses for this process agree well with the observed values (Table S27, and Fig. S22–S25†); we assume here the chemically most reasonable decomposition towards CuO in accordance with literature^{46,47} but mention that – astonishingly – also the presence of Cu_2S was observed (Fig. S25†). The origin of the latter remains mysterious for the

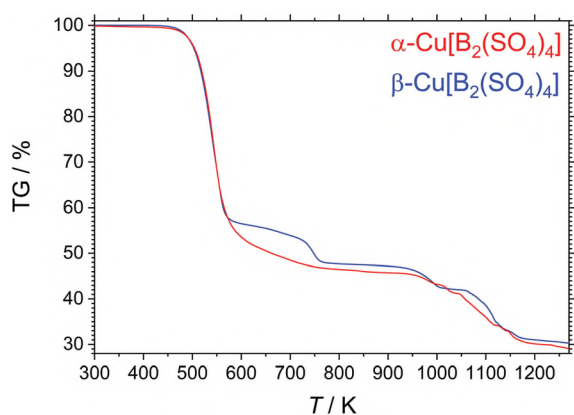
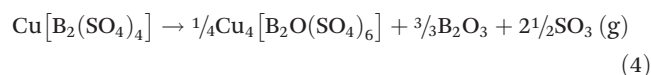


Fig. 6 Thermogravimetric analyses of $\alpha\text{-Cu}[\text{B}_2(\text{SO}_4)_4]$ and $\beta\text{-Cu}[\text{B}_2(\text{SO}_4)_4]$.

time being. For these steps, the decomposition of SO_3 to SO_2 and O_2 can be expected considering the temperature. This SO_2 might act as reducing agent for the formation of tiny amounts of Cu_2S . Powder diffraction depicted in Fig. S24† revealed CuB_2O_4 as a further intermediate presumably formed by the reaction of CuO and B_2O_3 . This behaviour is well-known from borosulfates.^{5,18} The competition and overlap of the processes forming CuO , CuB_2O_4 and Cu_2S between the second and third step in the TG curve (1000–1200 K) are responsible for the lack of another distinct step in the curve as well as the ambiguous DTA signal (Fig. S21†) in this temperature regime. In ambient air, a mixture of CuO and CuS is formed after heating $\beta\text{-Cu}[\text{B}_2(\text{SO}_4)_4]$ to 1270 K as depicted in Fig. S26.†

For $\beta\text{-Cu}[\text{B}_2(\text{SO}_4)_4]$, an additional decomposition step occurs prior to the formation of CuSO_4 indicating the evaporation of 2.5SO_3 (Fig. 6). In principle, this could indicate the formation of the hypothetical unconventional borosulfate $\text{Cu}_4[\text{B}_2\text{O}(\text{SO}_4)_6]$ analogous to the respective magnesium, manganese, cobalt, nickel, and zinc compounds¹⁸ comprising B–O–B bonds following the reaction equation:



The observed mass loss of 43.8 wt% and the expected value of 42.6 wt% agree fairly. However, both TPXRD (Fig. S22†) and powder diffraction on a sample heated at 570 K (Fig. S23†) revealed only the presence of CuSO_4 in this temperature regime and no diffraction pattern related to the additional phase indicated by TG. Additionally, syntheses analogous to the ones employed for $\text{M}_4[\text{B}_2\text{O}(\text{SO}_4)_6]$ ($\text{M} = \text{Mg}, \text{Mn}, \text{Co}, \text{Ni}, \text{Zn}$)¹⁸ with Cu , CuO or $\text{Cu}_2[(\text{OH})_2\text{CO}_3]$ as starting materials resulted in the sole formation of CuSO_4 , too. Again, this structure might be unstable due to the Jahn–Teller distortion making the formation of a dimer analogous to the M_2O_9 building unit in $\text{M}_4[\text{B}_2\text{O}(\text{SO}_4)_6]$ ($\text{M} = \text{Mg}, \text{Mn}, \text{Co}, \text{Ni}, \text{Zn}$) comprising two face-sharing CuO_6 octahedra highly unlikely or at least thermodynamically unstable.

Moreover, both polymorphs of $\text{Cu}[\text{B}_2(\text{SO}_4)_4]$ do not differ in their thermal stability according to our thermal analyses. Generally, a decrease in thermal stability of borosulfates is reported for higher condensed networks.^{5,11,18} The reason why this is not the case for $\text{Cu}[\text{B}_2(\text{SO}_4)_4]$ might again be found in the Jahn–Teller distortion and the cooperative effects.

For the sake of completeness, the thermal decomposition of $\text{Cu}[\text{B}(\text{SO}_4)_2(\text{HSO}_4)]$ was investigated, too. According to Fig. S27,† $\text{Cu}[\text{B}(\text{SO}_4)_2(\text{HSO}_4)]$ decomposes above 430 K *via* a similar process as $\text{Cu}[\text{B}_2(\text{SO}_4)_4]$ with the same intermediates CuSO_4 and $\text{Cu}_2\text{O}(\text{SO}_4)$ and the final product Cu_2S . The experimental and the expected mass losses match (Table S28†) as well as the temperature ranges of both $\text{Cu}[\text{B}(\text{SO}_4)_2(\text{HSO}_4)]$ and $\text{Cu}[\text{B}_2(\text{SO}_4)_4]$.

Experimental section

Syntheses

Both α -Cu[B₂(SO₄)₄] and β -Cu[B₂(SO₄)₄] were prepared solvothermally. 0.25 mmol Cu₂[(OH)₂CO₃] (Alfa Aesar, $\geq 55\%$ Cu) and 2 mmol H₃BO₃ (Merck, 99.5%) were loaded into a silica glass ampoule (length 15 cm, outer diameter: 1.2 cm, wall thickness: 0.1 cm) together with 1 ml oleum (VWR, 65% SO₃) or 0.5 ml oleum and 0.5 ml H₂SO₄ (Merck, 95–97%) for the syntheses of α -Cu[B₂(SO₄)₄] and β -Cu[B₂(SO₄)₄], respectively. Subsequently, the ampoule was fused and – without further aging – placed in a muffle furnace applying the following temperature program: heating to 450 K with 100 K h⁻¹, holding the temperature for 36 h, and cooling to room temperature with 6 K h⁻¹. Colourless crystals were obtained for both compounds. Ampoules were opened after cooling with liquid nitrogen (**Caution:** During and even after the reaction the ampoules are under remarkable pressure and must therefore be handled with care). After decantation of the excess sulfuric acid, the samples were washed with 5 ml anhydrous acetonitrile (Acros, 99.9%, extra dry) using a frit in a Schlenk line under nitrogen atmosphere. Afterwards, the product was transferred into an argon filled glovebox. The products are sensitive towards moisture and hence were stored under inert conditions for further investigations.

During handling we observed the highly hygroscopic nature of Cu[B₂(SO₄)₄]. The colourless compound reacts with moisture from air readily forming CuSO₄·H₂O (Fig. S28†). Consequently, the decomposition *via* hydrolysis is accompanied by an instant colour change to blue occurring within less than one minute when wielding the powder under non-inert conditions.

Cu[B(SO₄)₂(HSO₄)] was prepared solvothermally from 0.25 mmol Cu₂[(OH)₂CO₃], 1.6 mmol H₃BO₃, 0.5 ml oleum (65% SO₃) and 0.5H₂SO₄ by the same procedure as above solely changing the furnace temperature to 400 K.

Single-crystals of Cu(HSO₄)₂-I were obtained by a solvothermal synthesis. First, 2 mmol B(OH)₃ and 5 ml H₂SO₄ were mixed and stirred inside a nitrogen flushed Schlenk flask at 470 K for 1 h. Next, 2 ml oleum (65% SO₃) and 10 mmol metallic Cu (Aldrich, 99%) were added. After stirring the suspension for another hour at 470 K it was transferred into a silica glass ampoule. Subsequently, the ampoule was fused and placed in a muffle furnace at 670 K for 24 h with heating and cooling ramps of 200 K h⁻¹. The single-crystals of Cu(HSO₄)₂-II were synthesised alike starting from 1 mmol B(OH)₃, 5 ml H₂SO₄, 2 ml oleum (65% SO₃) and 1 mmol Cu and changing the heating program to 620 K for 72 h. Ampoules were opened after cooling with liquid nitrogen (**Caution:** During and even after the reaction the ampoules are under remarkable pressure and must therefore be handled with care) and the single-crystals were taken directly out of the ampoule.

Single-crystals of Cu[S₂O₇] were prepared solvothermally. Beforehand, 6.7 mmol CuO (Alfa Aesar, 99.7%) and 7.3 mmol B₂O₃ were ground, transferred into a corundum crucible and heated for 12 h at 1070 K inside a muffle furnace with ramps

of 200 K h⁻¹. 0.0746 g of the product – CuB₂O₄ with CuO and Cu₃B₂O₆ side phases according to powder XRD (Fig. S29†) – and 0.25 mmol B₂O₃ were ground and filled into a silica glass ampoule together with 0.5 ml H₂SO₄ and 0.5 ml oleum (65% SO₃). Subsequently, the ampoule was fused and – without further aging – placed in a muffle furnace applying the following temperature program: heating to 450 K with 100 K h⁻¹, holding the temperature for 36 h, and cooling to room temperature with 6 K h⁻¹. The product contained colourless and highly moisture-sensitive single-crystals of Cu[S₂O₇]. However, after washing as detailed above a mixture of α -Cu[B₂(SO₄)₄], β -Cu[B₂(SO₄)₄] and Cu[S₂O₇] was present according to powder XRD (Fig. S30†).

It is worth to say that for the successful preparation of both, Cu(HSO₄)₂ and Cu[S₂O₇], the addition of boron containing species appears to be crucial since analogous syntheses without it resulted in the solely formation of CuSO₄.

Single-crystal structure determination

Immediately after opening an ampoule, single-crystals were taken directly out of the mother liquid and transferred into perfluorinated polyether. Suitable single-crystals of Cu(HSO₄)₂-I, Cu(HSO₄)₂-II and β -Cu[B₂(SO₄)₄] were selected for single-crystal XRD under a polarising microscope. Diffraction data were collected with a Bruker D8 Venture diffractometer using Mo-K α radiation ($\lambda = 0.7093$ Å). Absorption correction was performed by the multi-scan method. The structures were solved by Direct Methods and refined by full-matrix least-squares technique with the SHELXTL crystallographic software package.⁴⁸ The hydrogen atoms were refined using residual density of electrons for localisation and a reasonable restraint for the length of the O–H bond.⁴⁹ All hydrogen atoms were assigned fixed isotropic displacement parameters equal to 1.2U_{eq} of the bonded oxygen atom. Relevant crystallographic data and further details of the structure determinations are summarised in Tables S3–S5, S10–S12 and S18–S20.†

Further details of the crystal structure investigations may be obtained at <https://www.ccdc.cam.ac.uk/on> quoting the depositary numbers CSD-2118186 (β -Cu[B₂(SO₄)₄]), CSD-2118185 (Cu(HSO₄)₂-I), CSD-2118183 (Cu(HSO₄)₂-II), CSD-2118184 (Cu[S₂O₇]), the names of the authors, and citation of this publication.

X-ray powder diffraction

The samples were ground and filled into a Hilgenberg glass capillary (outer diameter 0.3 mm, wall thickness 0.01 mm) inside an argon filled glovebox. The data were collected with a Bruker D8 Advance diffractometer with Cu-K α radiation ($\lambda = 1.54184$ Å) with a 1D LynxEye detector, steps of 0.02° and transmission geometry. The generator was driven at 40 kV and 40 mA. The background at lower diffraction angles is due to the absorption of the glass capillary.

Temperature-programmed X-Ray Powder Diffraction (TPXRD) was performed with the same device using a furnace attachment and a silica-glass Hilgenberg capillary (outer diameter 0.3 mm, wall thickness 0.01 mm). The strong back-

ground between $12.5^\circ < 2\theta < 30^\circ$ is due to the used furnace attachment.

The non-hygroscopic powders, *e.g.* decomposed Cu [B₂(SO₄)₄] (for further details see Thermal analysis) were measured with a Seifert 3003 TT diffractometer at room temperature in Bragg–Brentano geometry using Cu-K_α radiation ($\lambda = 1.54184 \text{ \AA}$), a GE METEOR 1D line detector and a Ni-Filter to suppress K_β radiation (X-ray tube operated at 40 kV and 40 mA, scan range: 5–80°, increment: 0.02°, 40 scans per data point, integration time: 200 s per degree, variable divergence slit).

Rietveld refinement

Analysis of diffraction data was performed using the Rietveld method with the program TOPAS V.⁵⁰ The instrumental resolution function was determined empirically from a set of fundamental parameters using a reference scan of Si (NIST 640d).⁵¹ The structural models of β-Cu[B₂(SO₄)₄] from our single-crystal XRD measurement, α-Cu[B₂(SO₄)₄] and Cu[B(SO₄)₂(HSO₄)] reported by Bruns *et al.*²² and CuSO₄ by Wildner and Giester⁵² were used as a starting models for Rietveld analysis. The isotropic displacement parameters were constrained to one common value for all atoms in order to minimise quantification errors. The parameters of the hydrogen atoms were not refined. Details are displayed in Tables S1 and S2.† Further details of the crystal structure investigations may be obtained at <https://www.ccdc.cam.ac.uk/> on quoting the depository numbers CSD-2118182 (α-Cu[B₂(SO₄)₄]) and CSD-2118180 (β-Cu[B₂(SO₄)₄]), the names of the authors, and citation of this publication.

FTIR spectroscopy

The Fourier-transform infrared spectra were recorded at room temperature with a Bruker EQUINOX 55 T-R spectrometer using a Platinum ATR device (scan range: 400–4000 cm⁻¹, resolution: 2 cm⁻¹, 32 scans per sample).

UV-Vis-NIR spectroscopy

UV-vis-NIR spectra were recorded as diffuse reflection spectra at room temperature on a PerkinElmer λ 750s spectrometer equipped with a Labsphere 60 mm RSA ASSY integrating sphere with a 0° d⁻¹ measuring geometry. Labsphere Spectralon SRS-99 was used as the white standard. Scan range: 200–1500 nm, increment 1 nm, scan rate: 120 nm min⁻¹.

Thermal analysis

The thermogravimetric (TG) and differential thermal (DTA) analyses were performed with a NETZSCH STA 409 PC Luxx thermobalance under nitrogen atmosphere with 70 mL min⁻¹ flow in alumina crucibles (heating rate: 10 K min⁻¹). The residues after these measurements were investigated by powder diffraction. Additionally, samples of both α-Cu[B₂(SO₄)₄] and β-Cu[B₂(SO₄)₄] were heat treated in order to investigate the thermal decomposition process in more detail. α-Cu[B₂(SO₄)₄] was heated for 10 h at 970 K in ambient air inside a corundum crucible using a muffle furnace. β-Cu[B₂(SO₄)₄] was heated for 10 h inside a corundum crucible using a tube furnace at 570 K

in nitrogen atmosphere with 70 mL min⁻¹ flow and at 1270 K in ambient air, respectively. The former product was handled under inert conditions.

Microscopy

Both α-Cu[B₂(SO₄)₄] and β-Cu[B₂(SO₄)₄] products were investigated by light microscopy both through the closed ampoule and after opening embedded in perfluorinated polyether. An Olympus IX70 Microscope with a Abrio CRi CCD camera was used.

Magnetic properties

The powdered samples of α-Cu[B₂(SO₄)₄] (1) and a mixture of 93% β-Cu[B₂(SO₄)₄] and 7% α-Cu[B₂(SO₄)₄] (2) were loaded into polyethylene (PE) capsules in an argon filled drybox and attached to the sample holder rod of a Vibrating Sample Magnetometer (VSM) for measuring the magnetization $M(T,H)$ in a Quantum Design Physical Property Measurement System (PPMS). The samples were investigated in the temperature range of 3–300 K with an applied external magnetic field of 10 kOe. The recorded susceptibilities were corrected by the diamagnetic contributions, calculated to $\chi_{\text{dia}}(\text{Cu[B}_2(\text{SO}_4)_4]) = -171.8 \times 10^{-6} \text{ emu mol}^{-1} (= 1 \times \chi(\text{Cu}^{2+}) + 2 \times \chi(\text{B}^{3+}) + 4 \times \chi(\text{SO}_4^{2-}) = -11.0 \times 10^{-6} \text{ emu mol}^{-1} + 2 \times -0.2 \times 10^{-6} \text{ emu mol}^{-1} + 4 \times -40.1 \times 10^{-6} \text{ emu mol}^{-1})$ using the increments tabulated in ref. 53.

DFT calculations

Quantum chemical calculations were performed in the framework of density functional theory (DFT) using a linear combination of Gaussian-type functions (LCGTF) scheme as implemented in CRYSTAL17.⁵⁴ Spin polarized (open shell) calculations were performed using the PBE⁵⁵ xc-functional with D3 dispersion correction.⁵⁶ Experimental structures of α-Cu [B₂(SO₄)₄], β-Cu[B₂(SO₄)₄] and α-Co[B₂(SO₄)₄] served as starting points for full structure relaxations. All-electron basis sets for Cu, B, S and O were taken from ref. 57. The outermost coefficient of the S basis set was modified to 0.515. The convergence criterion was set to 1×10^{-8} a.u. with a *k*-mesh sampling of $6 \times 6 \times 6$.

Further details of the crystal structure relaxations may be obtained at <https://www.ccdc.cam.ac.uk/> on quoting the depository numbers CSD-2118178 (α-Cu[B₂(SO₄)₄]), CSD-2118179 (β-Cu[B₂(SO₄)₄]) and 2118181 (γ-Cu[B₂(SO₄)₄]).

Conclusions

In this contribution, the two polymorphs α-Cu[B₂(SO₄)₄] and β-Cu[B₂(SO₄)₄] were prepared solvothermally. Their crystal structure was redetermined and determined for the first time, respectively. α-Cu[B₂(SO₄)₄] is composed of infinite chains of edge sharing supertetrahedra (1D anion) while β-Cu[B₂(SO₄)₄] forms 2D borosulfate anions comprised of *vierer* and *zwölfer* rings formed by alternately corner and edge sharing supertetrahedra. In both polymorphs, the Cu²⁺ cation is octahedrally

coordinated showing Jahn–Teller distortion resulting in elongated octahedra. The stability of the two polymorphs α -Cu[B₂(SO₄)₄] and β -Cu[B₂(SO₄)₄] was compared based on DFT. A third polymorph with a hypothetical structure isotypic to α -Co[B₂(SO₄)₄] (“cation between layers”) is energetically close to the known structures and can therefore be predicted. This model (γ -Cu[B₂(SO₄)₄]) features a rather unusual compressed CuO₆ octahedral geometry.

Further, the optical, magnetic and thermal properties of both polymorphs and the further copper borosulfate Cu[B(SO₄)₂(HSO₄)] were characterised extensively. The Cu²⁺ cations confirmed by magnetic measurements govern the UV-Vis-NIR spectra with three distinct d–d transitions revealing the weak coordination behaviour of the borosulfate anion. Thermally, Cu[B₂(SO₄)₄] and Cu[B(SO₄)₂(HSO₄)] decompose above 460 and 430 K, respectively.

Hence, the three borosulfates Cu[B(SO₄)₂(HSO₄)], α -Cu[B₂(SO₄)₄] and β -Cu[B₂(SO₄)₄] consist of cyclo- (0D), ino- (1D) and phyllosilicate-analogous (2D) anions, respectively. In other words, for one cation, namely copper, there are three borosulfate anions differing in their dimensionality. Additionally, Cu[B₂(SO₄)₄] is the first example in borosulfate chemistry of polymorphism with two polymorphs differing in the dimensionality of their borosulfate anion.

Author contributions

M. H. conducted all experiments and analyses not noted otherwise, solved the crystal structures of β -Cu[B₂(SO₄)₄] and Cu[S₂O₇], prepared all visualisation and wrote the original draft; F. P. conducted and analysed the DFT calculations; O. J. and R. P. conducted and analysed the magnetic measurements; H. T. prepared single-crystals of Cu(HSO₄)₂ and solved the crystal structures of both polymorphs with assistance from P. G.; H. A. H. supervised all the work. All authors reviewed and edited the final draft of the manuscript.

Conflicts of interest

There are no conflicts to declare.

Acknowledgements

H. A. H., M. H. and P. G. thank the Deutsche Forschungsgemeinschaft (DFG) for financial support under the project HO 4503/5-1.

References

- 1 S. G. Jantz, M. Dialer, L. Bayarjargal, B. Winkler, L. van Wüllen, F. Pielhofer, J. Brgoch, R. Weihrich and H. A. Höpfe, *Adv. Opt. Mater.*, 2018, 7, 1800497.
- 2 M. J. Schäfer, S. G. Jantz, F. Pielhofer and H. A. Höpfe, *Dalton Trans.*, 2019, 48, 10398–10402.
- 3 M. Hämmer, O. Janka, J. Bönninghausen, S. Klenner, R. Pöttgen and H. A. Höpfe, *Dalton Trans.*, 2020, 49, 8209–8225.
- 4 P. Netzsch, H. Bariss, L. Bayarjargal and H. A. Höpfe, *Dalton Trans.*, 2019, 48, 16377–16383.
- 5 P. Netzsch, M. Hämmer, P. Gross, H. Bariss, T. Block, L. Heletta, R. Pöttgen, J. Bruns, H. Huppertz and H. A. Höpfe, *Dalton Trans.*, 2019, 48, 4387–4397.
- 6 M. Hämmer, L. Bayarjargal and H. A. Höpfe, *Angew. Chem., Int. Ed.*, 2021, 60, 1503–1506.
- 7 Y. Li, Z. Zhou, S. Zhao, F. Liang, Q. Ding, J. Sun, Z. Lin, M. Hong and J. Luo, *Angew. Chem., Int. Ed.*, 2021, 60, 11457–11463.
- 8 H. A. Höpfe, K. Kazmierczak, M. Daub, K. Förg, F. Fuchs and H. Hillebrecht, *Angew. Chem., Int. Ed.*, 2012, 51, 6255–6257.
- 9 P. Netzsch and H. A. Höpfe, *Inorg. Chem.*, 2020, 59, 18102–18108.
- 10 P. Netzsch and H. A. Höpfe, *Z. Anorg. Allg. Chem.*, 2020, 646, 1563–1569.
- 11 P. Netzsch, F. Pielhofer, R. Glaum and H. A. Höpfe, *Chem. – Eur. J.*, 2020, 26, 14745–14753.
- 12 P. Netzsch, F. Pielhofer and H. A. Höpfe, *Inorg. Chem.*, 2020, 59, 15180–15188.
- 13 (a) J. Bruns, H. A. Höpfe, M. Daub, H. Hillebrecht and H. Huppertz, *Chem. – Eur. J.*, 2020, 26, 7966–7980; (b) P. Netzsch and H. A. Höpfe, *Eur. J. Inorg. Chem.*, 2021, 2021, 1065–1070.
- 14 L. C. Pasqualini, O. Janka, S. Olthof, H. Huppertz, K. R. Liedl, R. Pöttgen, M. Podewitz and J. Bruns, *Chem. – Eur. J.*, 2020, 26, 17405–17415.
- 15 P. Netzsch, R. Stroh, F. Pielhofer, I. Krossing and H. A. Höpfe, *Angew. Chem., Int. Ed.*, 2021, 60, 10643–10646.
- 16 F. Liebau, *Structural Chemistry of Silicates*, Springer, Heidelberg, 1985.
- 17 P. Gross, A. Kirhhain and H. A. Höpfe, *Angew. Chem., Int. Ed.*, 2016, 55, 4353–4355.
- 18 P. Netzsch, P. Gross, H. Takahashi and H. A. Höpfe, *Inorg. Chem.*, 2018, 57, 8530–8539.
- 19 L. Pauling, *J. Am. Chem. Soc.*, 1929, 51, 1010–1026.
- 20 W. Loewenstein, *Am. Mineral.*, 1954, 39, 92–96.
- 21 M. Daub, K. Kazmierczak, P. Gross, H. A. Höpfe and H. Hillebrecht, *Inorg. Chem.*, 2013, 52, 6011–6020.
- 22 J. Bruns, M. Podewitz, K. R. Liedl, O. Janka, R. Pöttgen and H. Huppertz, *Angew. Chem., Int. Ed.*, 2018, 57, 9548–9552.
- 23 P. C. Burns and F. C. Hawthorne, *Can. Mineral.*, 1996, 34, 1089–1105.
- 24 F. C. Hawthorne and M. A. Cooper, *Mineral. Mag.*, 2013, 77, 2901–2912.
- 25 H. A. Jahn and E. Teller, *Proc. R. Soc. London, Ser. A*, 1937, 161, 220–235.
- 26 M. Größ and R. Glaum, *Z. Kristallogr.*, 1997, 212, 2647.
- 27 U. Steiner and W. Reichelt, *Acta Crystallogr., Sect. C: Cryst. Struct. Commun.*, 1997, 53, 1371–1373.

- 28 T. Balić Žunić and E. Makovicky, *Acta Crystallogr., Sect. B: Struct. Sci.*, 1996, **52**, 78–81.
- 29 E. Makovicky and T. Balić-Žunić, *Acta Crystallogr., Sect. B: Struct. Sci.*, 1998, **54**, 766–773.
- 30 H. A. Höpfe, *J. Solid State Chem.*, 2009, **182**, 1786–1791.
- 31 R. Hoppe, *Angew. Chem., Int. Ed. Engl.*, 1966, **78**, 52–63.
- 32 R. Hoppe, *Angew. Chem., Int. Ed. Engl.*, 1970, **9**, 25–34.
- 33 R. Hübenthal, *MAPLE. Program for the Calculation of the Madelung Part of Lattice Energy*, Universität Gießen, Gießen, 1993.
- 34 R. Hoppe, *Z. Kristallogr.*, 1979, **150**, 23–52.
- 35 V. Zimmermann, Dissertation, Justus-Liebig-Universität, 2017.
- 36 J. Peters and B. Krebs, *Acta Crystallogr., Sect. B: Struct. Crystallogr. Cryst. Chem.*, 1982, **38**, 1270–1272.
- 37 M. A. Hitchman and T. D. Waite, *Inorg. Chem.*, 1976, **15**, 2150–2154.
- 38 R. W. G. Wyckoff, *Am. J. Sci.*, 1925, **s5-9**, 448–459.
- 39 L. C. Pasqualini, H. Huppertz and J. Bruns, *Inorganics*, 2019, **7**, 145.
- 40 R. D. Shannon, *Acta Crystallogr., Sect. A: Cryst. Phys., Diffraction, Theor. Gen. Crystallogr.*, 1976, **32**, 751–767.
- 41 J. Bruns, M. Podewitz, M. Schauerperl, B. Joachim, K. R. Liedl and H. Huppertz, *Chem. – Eur. J.*, 2017, **23**, 16773–16781.
- 42 (a) J. Ruiz-Fuertes, M. N. Sanz-Ortiz, J. González, F. Rodríguez, A. Segura and D. Errandonea, *J. Phys.: Conf. Ser.*, 2010, **215**, 12048; (b) R. Valiente and F. Rodríguez, *Phys. Rev. B: Condens. Matter Mater. Phys.*, 1999, **60**, 9423–9429.
- 43 B. N. Figgis and M. A. Hitchman, *Ligand field theory and its applications*, Wiley-VCH, New York, NY, 2000.
- 44 M. Wildner, G. Giester, M. Kersten and K. Langer, *Phys. Chem. Miner.*, 2014, **41**, 669–680.
- 45 (a) G. Accorsi, G. Verri, M. Bolognesi, N. Armaroli, C. Clementi, C. Miliani and A. Romani, *Chem. Commun.*, 2009, 3392–3394; (b) G. Pozza, D. Ajò, G. Chiari, F. de Zuane and M. Favaro, *J. Cult. Herit.*, 2000, **1**, 393–398.
- 46 L. Bald, M. Spiess, R. Gruehn and T. Kohlmann, *Z. Anorg. Allg. Chem.*, 1983, **498**, 153–160.
- 47 (a) A. M. Gadalla, *Int. J. Chem. Kinet.*, 1984, **16**, 655–668; (b) H. Tanaka and N. Koga, *J. Chem. Educ.*, 1990, **67**, 612.
- 48 G. M. Sheldrick, *Acta Crystallogr., Sect. C: Struct. Chem.*, 2015, **71**, 3–8.
- 49 T. Steiner, *Angew. Chem., Int. Ed.*, 2002, **41**, 48–76.
- 50 Bruker AXS, *Topas V5, General profile and structure analysis software for powder diffraction data. User's Manual*, Karlsruhe, Germany, 2014.
- 51 R. W. Cheary, A. A. Coelho and J. P. Cline, *J. Res. Natl. Inst. Stand. Technol.*, 2004, **109**, 1–25.
- 52 M. Wildner and G. Giester, *Mineral. Petrol.*, 1988, **39**, 201–209.
- 53 G. A. Bain and J. F. Berry, *J. Chem. Educ.*, 2008, **85**, 532.
- 54 (a) R. Dovesi, A. Erba, R. Orlando, C. M. Zicovich-Wilson, B. Civalleri, L. Maschio, M. Rérat, S. Casassa, J. Baima, S. Salustro and B. Kirtman, *Wiley Interdiscip. Rev.: Comput. Mol. Sci.*, 2018, **8**, e1360; (b) R. Dovesi, V. R. Saunders, C. Roetti, R. Orlando, C. M. Zicovich-Wilson, F. Pascale, B. Civalleri, K. Doll, N. M. Harrison, I. J. Bush, P. D'Arco, M. Llunell, M. Causà, J. Noël, L. Maschio, A. Erba, A. Rerat and S. Casassa, *CRYSTAL17 User's Manual*, University of Torino, Torino, 2017.
- 55 J. P. Perdew, K. Burke and M. Ernzerhof, *Phys. Rev. Lett.*, 1996, **77**, 3865–3868.
- 56 (a) S. Grimme, J. Antony, S. Ehrlich and H. Krieg, *J. Chem. Phys.*, 2010, **132**, 154104; (b) S. Grimme, S. Ehrlich and L. Goerigk, *J. Comput. Chem.*, 2011, **32**, 1456–1465; (c) S. Grimme, A. Hansen, J. G. Brandenburg and C. Bannwarth, *Chem. Rev.*, 2016, **116**, 5105–5154.
- 57 (a) K. Doll and N. M. Harrison, *Chem. Phys. Lett.*, 2000, **317**, 282–289; (b) R. Orlando, R. Dovesi, C. Roetti and V. R. Saunders, *J. Phys.: Condens. Matter*, 1990, **2**, 7769–7789; (c) A. Lichanot, E. Aprà and R. Dovesi, *Phys. Status Solidi*, 1993, **177**, 157–163; (d) J. Scaranto and S. Giorgianni, *J. Mol. Struct.: THEOCHEM*, 2008, **858**, 72–76.